JOURNAL OF THERMOPHYSICS AND HEAT TRANSFER
Vol. 21, No. 3, July–September 2007

Mathematical Modeling of Catalytic-Surface Combustion of Reacting Flows

Timothy W. Tong,* Mohsen M. Abou-Ellail,† and Yuan Li‡
George Washington University, Washington, D.C. 20052

DOI: 10.2514/1.27014

Catalytic combustion of methane–air mixtures involves the adsorption of the fuel and oxidant into a platinum surface, chemical reactions of the adsorbed species, and the desorption of the resulting products. Readsorption of some produced gases is also possible. The present paper is concerned with the numerical computation of heat transfer and chemical reactions in flowing methane–air mixtures impinging vertically on a platinum-coated hot plate. Seventy-three elementary reactions are included in the gas phase and in the solid platinum surface. The platinum surface temperature is fixed, whereas the properties of the reacting flow are computed. Finite-volume equations are solved iteratively for the reacting gas flow properties. In the platinum surface, surface species balance equations under steady-state conditions are solved numerically. The agreement with existing numerical data is fairly good for all main combustion products, whereas differences are observed for the rare species such as CO, O, H, HO_2, and CH_2O. The accuracy of the present results is accessed by checking the balance of the carbon element in the present carbon-containing compounds and similar published numerical data. The computational results for chemical reactions and mass transfer at the gas–surface interface are correlated by nondimensional relations.

Nomenclature

a_n	=	finite difference coefficients due to combined convection and diffusion
C_p	=	constant-pressure specific heat
h_g	=	gas-sensible enthalpy
k_{fj}	=	forward kinetic rate constants of reaction j
K_s	=	total number of elementary surface reactions
M	=	molecular weight
N_g	=	number of gas-phase species
N_s	=	number of surface species
P	=	gas pressure
R	=	universal gas constant
Re	=	Reynolds number
Sh	=	Sherwood number
$\dot{s}_k$	=	surface production or depletion rate in $\mathrm{mol/cm^2/s}$ of the surface species k
T_g	=	temperature of gas
u_i	=	velocity in direction i
V_{in}	=	inlet jet-centerline velocity
W_j	=	reaction rate of reaction j
$[X_k]$	=	generalized concentration of species k (gas phase: $\mathrm{mol/cm^3}$, surface phase: $\mathrm{mol/cm^2}$)
x	=	distance along the axial axis
x_i	=	distance along direction i
Y	=	species mass fraction
Z	=	surface site concentration
z_k	=	surface site fraction of species k (surface-coverage fraction)
Γ_h	=	thermal diffusivity
γ	=	sticking coefficient
δ	=	reaction boundary-layer thickness
μ	=	dynamic viscosity
ν_{lj}	=	stoichiometric coefficient of species l in reaction j
ρ	=	gas density

Presented as Paper 3815 at the 9th AIAA/ASME Joint Thermophysics and Heat Transfer Conference, San Francisco, CA, 5–8 June 2006; received 3 August 2006; revision received 18 October 2006; accepted for publication 19 October 2006.

*Dean, School of Engineering and Applied Science, 725 23rd Street, Northwest. Associate Fellow AIAA.

†Visiting Professor, School of Engineering and Applied Science, 725 23rd Street, Northwest. Member AIAA.

‡Graduate Research Assistant, School of Engineering and Applied Science, 725 23rd Street, Northwest.

I. Introduction

CATALYSTS have been widely used in many industrial applications to control the process of chemical reaction. One of the applications of catalysts is catalytic combustion. With the assistance of catalysts, the ignition temperature of fuel is lower than the ignition temperature of the fuel without catalysts. Combustion of methane at lower temperature can reduce emissions of pollutants, which is one of the most important advantages of catalytic combustion. Platinum and palladium are common catalysts used to assist combustion. Combustion of several fuels (i.e., a NH_3, CH_4, C_3H_8, and NH_3-CH_4 mixture) on a platinum surface in stagnation flowfield was studied experimentally by Williams et al. [1]. In addition, combustion of methane on a platinum surface was studied numerically by Song et al. [2]. In [2], the surface reaction of methane over platinum was modeled by a global reaction mechanism. Similarly, combustion of hydrogen on a platinum surface in a stagnation flowfield and a boundary-layer flowfield were studied numerically by Warnatz et al. [3]. In [3], elementary reaction mechanism of oxidation of hydrogen on a platinum surface, including reactions of absorption/desorption of reactant and products and reactions of surface radical recombination, was established and used in the model. Thermochemical data of surface species involved in the surface reactions were also published in [3]. Later, the elementary surface reaction mechanism of methane with platinum was established by Deutschmann et al. [4]. The detailed surface reaction mechanism was used by Deutschmann et al. to numerically simulate the experiments of surface combustion of methane over platinum conducted by Williams et al. [1]. It was found in [4] that methane is ignited at a surface temperature of around 1000 K and the reaction is fast between surface temperatures of 1000 and 1300 K; for surface temperatures below 1000 K, the surface reaction is slow and methane could not be ignited. Surface coverage of surface species and mole fractions of gas-phase species were calculated in [4]. Raja et al. [5] used the detailed surface mechanisms for methane combustion developed by Deutschmann et al. [4] to model the catalytic honeycomb monolith combustion.

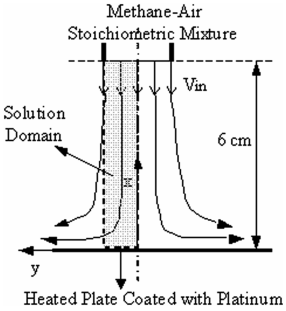

Fig. 1 Layout of impinging flow with surface reactions.

In the present paper, catalytic combustion of impinging methane–air mixtures is modeled numerically. The flow configuration is shown in Fig. 1. Unity equivalence ratio is used for the methane–air mixtures that impinge vertically over a flat hot plate. The surface of the flat plate is coated with platinum. The surface temperature of the flat plate is kept uniform, constant, and high enough to initiate catalytic combustion of the fuel–air mixture. The fuel and oxygen are consumed, whereas products are generated at the hot catalytic surface through surface reactions. The present two-dimensional model of impinging jet flow with surface reactions is developed. A multistep reaction mechanism is adopted for gas-phase reactions. It involves 49 elementary reactions and 16 chemical species for methane–air mixtures. The surface reaction mechanism developed by Deutschmann et al. [4] is adopted in the present work. This surface reaction mechanism for methane–air mixtures consists of 24 elementary surface reactions that involve 7 gas-phase species and 9 surface species. The surface reaction model developed by Coltrin et al. [6] is also invoked in the present work. Nondimensional relations are developed to represent the mass transfer and reaction rates at the gas–surface interface.

II. Mathematical Model and Solution Procedure

The numerical model for laminar flow, heat transfer, gas-phase combustion, and catalytic-surface reactions are presented in this section. The flow configuration is shown in Fig. 1. The model can be classified into four main groups of equations as follows:

A. Continuity and Momentum Equations

The mass continuity of reacting flows may be written as

$$\frac{\partial(\rho)}{\partial t} + \frac{\partial(\rho u_i)}{\partial x_i} = 0 \tag{1}$$

The momentum equation for the laminar reacting flow may be written in Cartesian tensor notations as (Abou-Ellail et al. [7])

$$\frac{\partial(\rho u_j)}{\partial t} + \frac{\partial}{\partial x_i}(\rho u_j u_i) - \frac{\partial}{\partial x_i}\left(\mu \frac{\partial u_j}{\partial x_i}\right) = -\frac{\partial(P)}{\partial x_j} + \frac{\partial}{\partial x_i}\left[\mu\left(\frac{\partial u_i}{\partial x_j} - \frac{2}{3}\frac{\partial u_k}{\partial x_k}\delta_{ij}\right)\right] \tag{2}$$

where u_j is the gas velocity along coordinate x_j. The impinging flow of Fig. 1 has a vertical axis of symmetry. The gravity force, which is pointing toward the negative x coordinate, is neglected in the present study, as can be seen from Eq. (2). However, if P represents hydrodynamic pressure, then the gravity force can be omitted from the momentum equation, to be replaced by a buoyancy force that is also neglected in the present axially symmetric impinging vertical flow.

B. Energy Equations

The energy equation for the reacting flow is

$$\frac{\partial \rho h_g}{\partial t} + \frac{\partial}{\partial x_i}(\rho u_i h_g) - \frac{\partial}{\partial x_i}\left(\Gamma_h \frac{\partial h_g}{\partial x_i}\right) = -\sum_j (\Delta H_j) W_j \tag{3}$$

where ΔH_j and W_j are the enthalpy of reaction and reaction rate of chemical reaction j of the reaction mechanism involving methane–air mixtures (Table 1). In the preceding equations, the subscripts g denote gas phase. The gas temperature, at any point, is directly related to the local gas-sensible enthalpy, gas species mass fractions Y_j, and constant-pressure specific heats, namely:

$$h_g = \int \left(\sum_j C_{pj} Y_j\right) \mathrm{d}T \tag{4}$$

The lower limit of the preceding integration is 298 K, and the upper limit equals T_g.

C. Species Mass Fraction Equations

The species mass fractions in reacting flows may be written as

$$\frac{\partial(\rho Y_l)}{\partial t} + \frac{\partial(\rho u_i Y_l)}{\partial x_i} - \frac{\partial}{\partial x_i}\left(\Gamma_{Y_l} \frac{\partial Y_l}{\partial x_i}\right) = M_l \sum_j \nu_{lj} W_j \tag{5}$$

where Y_l is the mass fraction of species l and Γ_{Yl} is its molecular diffusivity, and M_l is the molecular mass of species l. The rates of production of the chemical species , W_j, in Eq. (3) may be written as

$$W_j = A_j T^{\alpha_j} \exp\left(-\frac{E_j}{RT_g}\right) \prod_{\kappa=1}^{N} \left(\frac{\rho Y_\kappa}{M_\kappa}\right)^{\upsilon'_{ij}} \tag{5a}$$

where A_j is the frequency factor, α_j is the preexponential temperature exponent, and E_j is the activation energy of reaction j (as given in Table 1), υ'_{ij} are the reactants' stoichiometric coefficients, M_k is the molecular weight of species k, and N is the number of reacting gas species involved. As shown in Table 1, this mechanism consists of 49 elementary reactions, which is a compromise between the full reaction and the skeletal reaction mechanisms. The reaction mechanism is based on depolymerizing the complex molecule of methane into simpler intermediate hydrocarbon molecules. The chemical kinetic mechanism involves 16 species, namely: CH_4, CH_3, CH_2, CH, CH_2O, CHO, CO, CO_2, O_2, O, OH, H, H_2, H_2O, HO_2, and H_2O_2; the 49 involved elementary reactions are discussed in detail by Tong et al. [8] and Peters [9,10]. It should be mentioned here that ν_{lj} is taken as a positive value for products and negative for reactants, as required for proper summation of the effect of each reaction on the production of a particular species. The thermodynamic data needed in the present computations can be found from CHEMKIN [11]. The gas physical properties are taken as temperature-dependent. The density is computed from the ideal gas equation of state, whereas the species constant-pressure specific heats and gas viscosity are computed from standard temperature polynomials. The remaining gas physical properties can then be obtained from the preceding physical properties, which are involved in Prandtl and Lewis numbers. In the present work, the gas Prandtl number is equal to 0.7 and the unity Lewis number is assumed. It should be mentioned here that most combustion products have a nearly unity Lewis number, expect for gases with lower molecular weights such as H and H_2, which are rare species in methane–air combustion products. Moreover, for forced-convection flows, diffusion is of secondary importance.

D. Surface Reactions

For a steady-state problem, the solution has no change with respect to time. Thus, surface coverage of any surface species with respect to time is zero. The variation of the surface coverage with respect to time can be computed from the net production of each surface species. The conservation of the surface coverage of species k may be

Table 1 Gas-phase reaction mechanism

No.	Reaction	A_j, mol, cm^3, s	α_j	E_j, kJ/mol
1f	$O_2 + H \rightarrow OH + O$	2.000×10^{14}	0.00	70.30
1b	$OH + O \rightarrow O_2 + H$	1.568×10^{13}	0.00	3.52
2f	$H_2 + O \rightarrow OH + H$	5.060×10^{04}	2.67	26.3
2b	$OH + H \rightarrow H_2 + O$	2.222×10^{4}	2.67	18.29
3f	$H_2 + OH \rightarrow H_2O + H$	1.000×10^{8}	1.60	13.8
3b	$H_2O + H \rightarrow H_2 + OH$	4.312×10^{8}	1.60	76.46
4f	$OH + OH \rightarrow H_2O + O$	1.500×10^{9}	1.14	0.42
4b	$H_2O + O \rightarrow OH + OH$	1.473×10^{10}	1.14	71.09
5f	$O_2 + H + M \rightarrow HO_2 + M$	2.300×10^{18}	−0.80	0.00
5b	$HO_2 + M \rightarrow O_2 + H + M$	3.190×10^{18}	−0.80	195.39
6	$HO_2 + H \rightarrow OH + OH$	1.500×10^{14}	0.00	4.20
7	$HO_2 + H \rightarrow H_2 + O_2$	2.500×10^{13}	0.00	2.90
8	$HO_2 + OH \rightarrow H_2O + O_2$	6.000×10^{13}	0.00	0.00
9	$HO_2 + H \rightarrow H_2O + O$	3.000×10^{13}	0.00	7.20
10	$HO_2 + O \rightarrow OH + O_2$	1.800×10^{13}	0.00	−1.70
11	$HO_2 + HO_2 \rightarrow H_2O_2 + O_2$	2.500×10^{11}	0.00	−5.20
12f	$OH + OH + M \rightarrow H_2O_2 + M$	3.250×10^{22}	−2.00	0.00
12b	$H_2O_2 + M \rightarrow OH + OH + M$	1.692×10^{24}	−2.00	202.29
13	$H_2O_2 + H \rightarrow H_2O + OH$	1.000×10^{13}	0.00	15.00
14f	$H_2O_2 + OH \rightarrow H_2O + HO_2$	5.400×10^{12}	0.00	4.20
14b	$H_2O + HO_2 \rightarrow H_2O_2 + OH$	1.802×10^{13}	0.00	134.75
15	$H + H + M \rightarrow H_2 + M$	1.800×10^{18}	−1.00	0.00
16	$OH + H + M \rightarrow H_2O + M$	2.200×10^{22}	−2.00	0.00
17	$O + O + M \rightarrow O_2 + M$	2.900×10^{17}	−1.00	0.00
18f	$CO + OH \rightarrow CO_2 + H$	4.400×10^{6}	1.50	−3.1
18b	$CO_2 + H \rightarrow CO + OH$	4.960×10^{8}	1.50	89.71
19f	$CH_4 + H \rightarrow H_2 + CH_3$	2.200×10^{4}	3.00	36.6
19b	$H_2 + CH_3 \rightarrow CH_4 + H$	8.830×10^{2}	3.00	33.53
20	$CH_4 + OH \rightarrow H_2O + CH_3$	1.600×10^{6}	2.10	10.3
21	$CH_3 + O \rightarrow CH_2O + H$	7.000×10^{13}	0.00	0.00
22	$CH_3 + OH \rightarrow CH_2O + H + H$	9.000×10^{14}	0.00	64.8
23	$CH_3 + OH \rightarrow CH_2O + H_2$	8.000×10^{12}	0.00	0.00
24	$CH_3 + H \rightarrow CH_4$	6.000×10^{16}	−1.00	0.00
25	$CH_2O + H \rightarrow CHO + H_2$	2.500×10^{13}	0.00	16.7
26	$CH_2O + OH \rightarrow CHO + H_2O$	3.000×10^{13}	0.00	5.0
27	$CHO + H \rightarrow CO + H_2$	2.000×10^{14}	0.00	0.00
28	$CHO + OH \rightarrow CO + H_2O$	1.000×10^{14}	0.00	0.00
29	$CHO + O_2 \rightarrow CO + HO_2$	3.000×10^{12}	0.00	0.00
30	$CHO + M \rightarrow CO + H + M$	7.100×10^{14}	0.00	70.3
31	$CH_3 + H \rightarrow CH_2 + H_2$	1.800×10^{14}	0.00	63.0
32	$CH_2 + O_2 \rightarrow CO_2 + H + H$	6.500×10^{12}	0.00	6.3
33	$CH_2 + O_2 \rightarrow CO + OH + H$	6.500×10^{12}	0.00	6.3
34f	$CH_2 + H \rightarrow CH + H_2$	4.000×10^{13}	0.00	0.00
34b	$CH + H_2 \rightarrow CH_2 + H$	2.790×10^{13}	0.00	12.6
35	$CH + O_2 \rightarrow CHO + O$	3.000×10^{13}	0.00	0.00
36	$CH_3 + OH \rightarrow CH_2 + H_2O$	1.500×10^{13}	0.00	20.93
37	$CH_2 + OH \rightarrow CH_2O + H$	2.500×10^{13}	0.00	0.00
38	$CH_2 + OH \rightarrow CH + H_2O$	4.500×10^{13}	0.00	12.56
39	$CH + OH \rightarrow CHO + H$	3.000×10^{13}	0.00	0.00

written as (Warnatz et al. [3])

$$\frac{\mathrm{d}z_k}{\mathrm{d}t} = \frac{\dot{s}_k}{Z} \tag{6}$$

where Z is the total surface site density, and the surface density used in the present paper is 1.63×10^{15} cm^{-2} (Deutschmann et al. [4]).

Because the present reacting flow includes gas–surface interactions, the mass transfer between the gas phase and the catalytic surface needs to be included while solving the species mass fractions of the flowing gas. The mass fluxes transferred through the convection and diffusion process at the gas–surface interface of any gas-phase species are balanced by the production or depletion rates of that species by surface reactions. The surface boundary condition of each gas-phase species k based on the mass balance is given by Coltrin et al. [6] as

$$n \cdot [\rho Y_k (V_k + u)] = \dot{s}_k M_k \tag{7}$$

where n is the unit normal vector pointing outward to the surface, u is the bulk fluid velocity, and V_k is the diffusion velocity.

The production rate of each species $\dot{s}_k$, either gas-phase species or surface species, may be written as (Deutschmann et al. [12]):

$$\dot{s}_k = \sum_{j=1}^{K_s} \nu_{kj} k_{f_j} \prod_{k=1}^{N_g+N_s} [X_k]^{\nu'_{kj}} \tag{8}$$

where ν'_{kj} is left-hand side stoichiometric coefficients of the reaction equation, ν_{kj} is the right-hand side minus left-hand side stoichiometric coefficients of the reaction equation, $[X_k]$ is the species concentrations, and the units of gas-phase species and surface species concentrations are mol/cm^3 and mol/cm^2, respectively.

A detailed surface reaction mechanism is used to model the gas–surface interaction between the fuel and platinum. The surface reaction mechanism adopted in the present work, for methane–air mixtures reacting over platinum-coated surfaces, is established by Deutschmann et al. [4]; it is shown in Table 2. Deutschmann et al. analyzed the uncertainties in the surface reaction mechanism shown in Table 2. Deutschmann et al. rationalized the use of preexponential constants that are obtained either experimentally or through quantum-mechanical analytical studies. The surface chemical

Table 2 Surface reaction mechanism (Deutschmann et al. [4])

No.	Reaction	A_j, mol, cm^3, s	E_j, kJ/mol	Sticking coeff.
1	$H_2 + P_t(s) + P_t(s) \rightarrow H(s) + H(s)$			0.046
2	$H(s) + H(s) \rightarrow P_t(s) + P_t(s) + H_2$	1.0×10^{21}	67.4	
3	$O_2 + P_t(s) + P_t(s) \rightarrow O(s) + O(s)$			0.023
4	$O(s) + O(s) \rightarrow P_t(s) + P_t(s) + O_2$	1.0×10^{21}	213.2	
5	$H_2O + P_t(s) \rightarrow H_2O(s)$			0.75
6	$H_2O(s) \rightarrow H_2O + P_t(s)$	1.0×10^{13}	40.3	
7	$OH + P_t(s) \rightarrow OH(s)$			1
8	$OH(s) \rightarrow OH + P_t(s)$	1.0×10^{13}	192.8	
9	$CO + P_t(s) \rightarrow CO(s)$			0.84
10	$CO(s) \rightarrow CO + P_t(s)$	1.0×10^{13}	152.5	
11	$CH_4 + P_t(s) + P_t(s) \rightarrow CH_3(s) + H(s)$			0.01
12,13	$O(s) + H(s) \leftrightarrow OH(s) + P_t(s)$	1.0×10^{21}	11.5	
14,15	$H(s) + OH(s) \leftrightarrow H_2O(s) + P_t(s)$	1.0×10^{21}	17.4	
16,17	$OH(s) + OH(s) \leftrightarrow H_2O(s) + O(s)$	1.0×10^{21}	48.2	
18,19	$CO(s) + O(s) \leftrightarrow CO_2 + P_t(s) + P_t(s)$	1.0×10^{21}	105	
20	$C(s) + O(s) \rightarrow CO(s) + P_t(s)$	1.0×10^{21}	62.8	
21	$CO(s) + P_t(s) \rightarrow C(s) + O(s)$	1.0×10^{18}	156.5	
22	$CH_3(s) + P_t(s) \rightarrow CH_2(s) + H(s)$	1.0×10^{21}	20	
23	$CH_2(s) + P_t(s) \rightarrow CH(s) + H(s)$	1.0×10^{21}	20	
24	$CH(s) + P_t(s) \rightarrow C(s) + H(s)$	1.0×10^{21}	20	

species are denoted by a label (s), as shown in Table 2. The surface reaction mechanism consists of 24 elementary reactions and involves seven gas-phase species (namely, CH_4, CO, CO_2, O_2, OH, H_2, and H_2O) and nine surface species [namely, $CH_3(s)$, $CH_2(s)$, CH(s), CO (s), C(s), O(s), OH(s), H(s), and $P_t(s)$]. The reaction-rate constants are described in terms of either Arrhenius expression or a sticking coefficient. The Arrhenius expression form is

$$k_{fj} = A_j \exp\left(\frac{-E_j}{RT}\right) \tag{9}$$

The sticking coefficient can be converted to the usual kinetic rate constants via the relation given by Coltrin et al. [6]:

$$k_{fj} = \frac{\gamma}{1 - \gamma/2} \frac{1}{Z^m} \sqrt{\frac{RT_g}{2\pi M}} \tag{10}$$

where m is the sum of the surface reactants' stoichiometric coefficient and M is the molecular weight of the gas-phase species. The thermochemical data needed to determined the rate coefficients for the reverse reactions and enthalpies of the surface species are provided by Warnatz et al. [3].

E. Numerical Solution Procedure

The two-dimensional flow over the catalytic surface, shown in Fig. 1, is overlaid with a finite grid of nodes. At each nodal point, Eqs. (2), (3), and (5) and the pressure-correction counterpart of Eq. (1) are formally integrated over a control volume surrounding this nodal point. The faces of the control volume bisect the distances between the particular node and the four nearest neighbor nodes. The formal integration is performed with due care to preserve the physical meaning and overall balance of each dependent variable. The final form of the finite difference equations are written as follows (Abou-Ellail et al. [7]):

$$\left(\sum(a_n) - S_P\right)\Psi_P = \sum(a_n \Psi_n) + S_u \tag{11}$$

where Ψ stands for any of the dependent variables, namely: axial and radial velocity components, gas-sensible enthalpy, species mass fractions, or the pressure correction that is used to satisfy both mass continuity and momentum equations simultaneously. The summation $\sum$ is over the four neighbors n of a typical node p. The preceding finite difference coefficients a_n are computed using the upwind method, such that these coefficients are always nonnegative to give the proper combined effects of convection and diffusion. S_p and S_u are the coefficients of the integrated source term at node p.

The solution procedure is based on the line-by-line, alternating-direction, tridiagonal matrix algorithm (TDMA). This solution procedure is based on solving each line of nodes as a tridiagonal matrix, then sweeping the whole computational grid by sequentially solving the adjacent lines. Details of the preceding algorithm are given by Abou-Ellail et al. [7]. The difference equations (11) for each dependent variable are modified at the boundaries of the solution domain, shown in Fig. 1, to impose the conditions there. The number of nodes along the x axis is 302, because most of the changes occur axially. However, only ten transverse nodes can be used to cover the jet inlet section. On the flat-plate surface, the velocity components vanish, whereas all other dependent variables' normal gradients reflect the mass and heat fluxes due to surface reactions, as dictated by Eq. (7). Along the jet axis of symmetry, the normal gradient is equal to zero for all variables except the transverse velocity, which itself equals to zero. Along the axial nodes adjoining the jet boundary, the normal gradients of all variables are equal to zero. At the inlet section, all variables are known from the specified incoming impinging jet conditions. Within each computational loop of the gas phase, Eq. (6) is solved iteratively for all surface species concentrations over the catalytic surface for the case of steady-state conditions, that is, $\mathrm{d}(z_k)/\mathrm{d}t = 0$. At the jet axis of symmetry, the transverse velocity is equal to zero. One thousand outer iterations were required for complete conversion of the gas-phase equations of the main gaseous components. On the other hand, within each outer iteration, 200 inner iterations were necessary for the surface species to converge without any appreciable fluctuations. An additional 1000 iterations were performed to assure the conversion and stability of the intermediate and rare species such as CO and CH_2O.

III. Presentation and Discussion of Results

The methane–air mixture flow of uniform velocity impinges at an angle of 90 deg onto a hot flat plate coated by platinum. The impinging jet exit section is 6 cm from the catalytic surface, as depicted in Fig. 1. In addition to the inlet velocity of 6 cm/s used by Deutschmann et al. [4], inlet velocities of 12, 24, 48, and 96 cm/s are used in the present computations to study the influence of inlet velocity on surface reactions. The computed Reynolds numbers corresponding to the preceding inlet velocities are 53.4, 106.8, 213.6, 427.2, and 854.4. The momentum, heat, and mass transfer of the impinging flowfield, as well as the catalytic reactions at the surface, are computed for each inlet velocity. In the present numerical simulations, the equivalence ratio of the fuel and air mixture at the inlet is equal to 1.0 and the inlet temperature of the gas mixture is

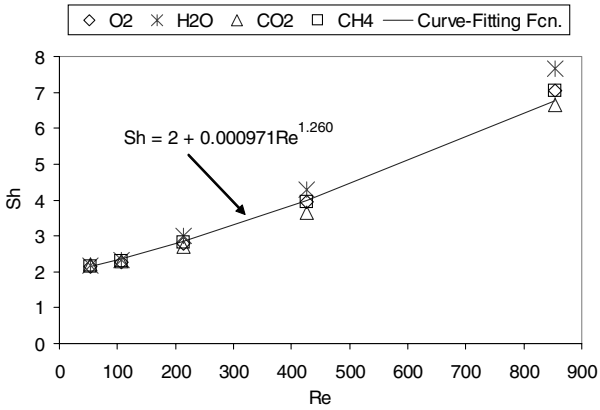

Fig. 2 Sherwood number versus Reynolds number for different inlet velocities.

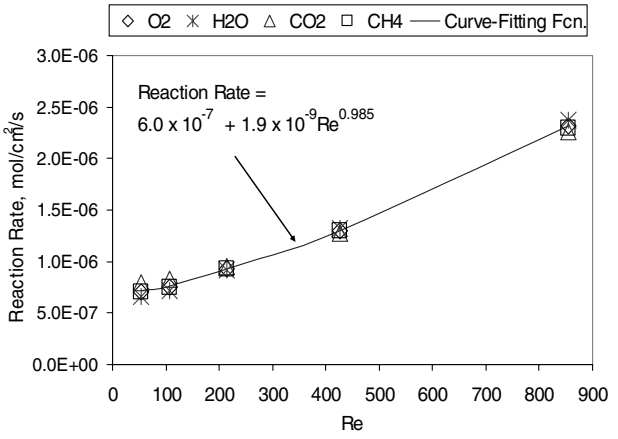

Fig. 3 Reaction rate versus Reynolds number for different inlet velocities.

300 K. The flat-plate surface temperature is fixed at 1150 K in the present simulations. The computational results, which include mass transfer, reaction rate of surface reaction, the surface species coverage, the mole fractions of gas species, and temperature profiles, are presented in this section.

The Sherwood number is used as representative of the mass transfer of species between the reacting gas-phase and the platinum-surface species that take part in the heterogeneous reactions. The Sherwood number of the major species O_2, H_2O, CO_2, and CH_4 is computed at different Reynolds numbers. The Sherwood number of these major species is plotted versus the Reynolds number, as shown in Fig. 2. The numerical results show that at a fixed value of Reynolds number, the difference among the values of the major species' Sherwood numbers is small enough to allow a unique equation for Sherwood number versus Reynolds number. Thus, at a fixed Reynolds number, the value of the Sherwood number of all the major species can fairly be represented by one mean value. With this approximation, the relation between the Sherwood number of major species and the Reynolds number can be correlated into a single exponential function using curve-fitting methods. For the impinging flow configuration, the relation between the Sherwood number and the Reynolds number is correlated as

$$Sh = 2 + 0.000971Re^{1.260} \tag{12}$$

The preceding correlation is also plotted in Fig. 2. It can be concluded from Fig. 2 that the mass transfer of major species between the gas and surface species increases as the inlet velocity increases. Similarly, the reaction rates of the major species at a fixed value of Reynolds number can also be approximated by a mean value. The relation between the surface reaction rate ($\mathrm{mol/cm^2/s}$) and Reynolds number is correlated as

$$\text{reaction rate} = 6.0 \times 10^{-7} + 1.9 \times 10^{-9} Re^{0.985} \tag{13}$$

The computed values of reaction rates and the curve-fitting function of reaction rate are plotted in Fig. 3. It can be seen from Fig. 3 that surface reactions are more active at higher inlet velocities. The correlation in Eq. (13) shows that the rate of reaction increases almost linearly with the Reynolds number. Equation (13) implies that at 1150 K and unity equivalence ratio, methane–air mixtures react on catalytic surfaces as a one-step global reaction, given as $CH_4 + 2O_2 \rightarrow CO_2 + 2H_2O$, with a reaction rate computed from the preceding correlation. Needless to say that the constants of Eq. (13) are dependent on the surface temperature and the equivalence ratio.

Figure 4 shows the surface coverage of different surface species versus Reynolds number. The numerical data points of Deutschmann et al. [4] are also plotted in Fig. 4 for comparison. Figure 4 shows fairly good agreement between the present surface coverage of surface species and the surface coverage of Deutschmann et al. for an inlet velocity of 6 cm/s and surface temperature of 1150 K. Figure 4 shows that when fuel is ignited and the surface reactions reach steady

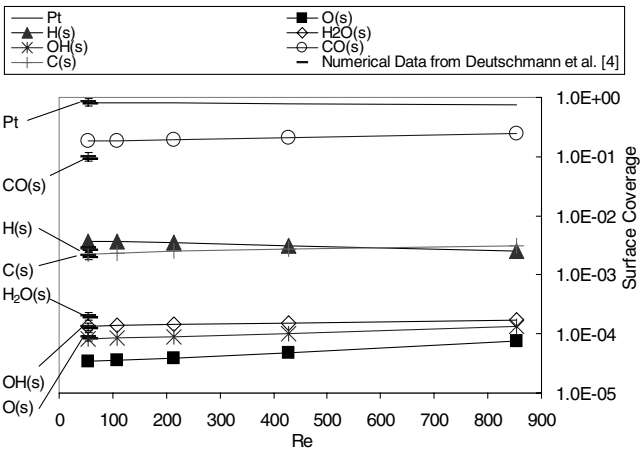

Fig. 4 Surface coverage at different inlet velocities.

state, most of the catalytic surface is covered with active platinum sites for all Reynolds numbers. The surface coverage of other surface species is small. The numerical model in this paper also predicts the same descending order of surface coverage; P_t(s) has highest surface coverage, CO(s) has the second highest surface coverage, and so on, whereas O(s) has the lowest surface coverage, exactly as predicted numerically by Deutschmann et al.

Figures 5 and 6 show species mole fractions versus the distances above the surface, along the jet axis of symmetry, at an inlet velocity of 6 cm/s ($Re = 53.4$). The numerical data of Deutschmann et al. [4] are also plotted for comparison. Figure 5 shows the mole fraction

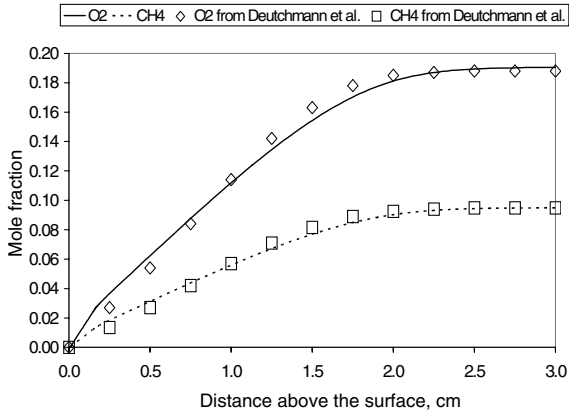

Fig. 5 Mole fractions of O_2 and CH_4 above the surface and comparisons with results of Deutschmann et al. [4], at 1150 K and $Re = 53.4$.

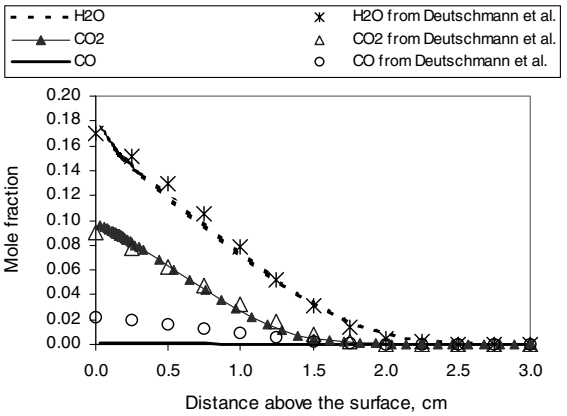

Fig. 6 Mole fractions of H_2O, CO_2 and CO above the surface and comparisons with results of Deutschmann et al. [4].

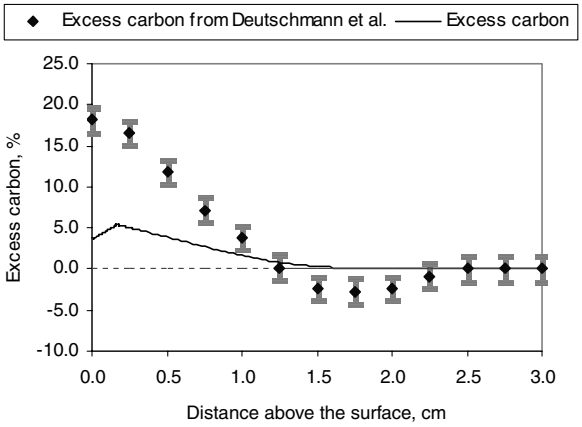

Fig. 7 Excess Carbon above the surface and comparisons with results of Deutschmann et al. [4].

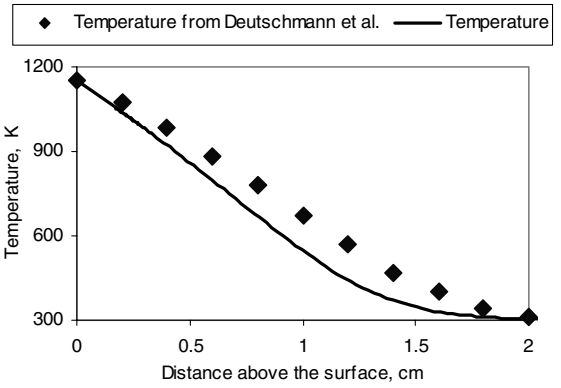

Fig. 8 Temperature profiles above the surface and comparisons with results of Deutschmann et al. [4].

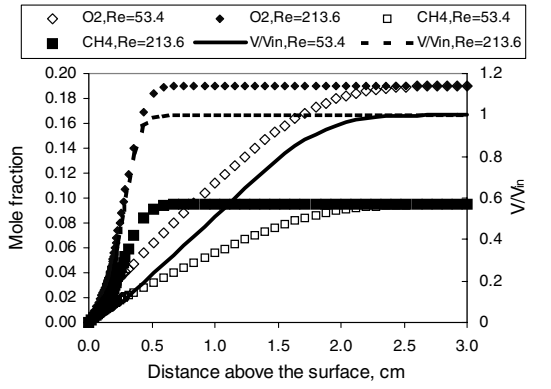

Fig. 9 Comparison of reactants' mole fractions and velocity profiles for $Re = 53.4$ ($V_{in} = 6$ cm/s) and $Re = 213.6$ ($V_{in} = 24$ cm/s), at 1150 K.

profiles of O_2 and CH_4. As shown in Fig. 5, for equivalence ratio of 1.0, the oxygen and methane are completely consumed at the catalytic surface. The mole fraction profiles of major combustion products are shown in Fig. 6. The numerical results computed by the present model agree well with the results of Deutschmann et al. for all species except the carbon monoxide. The present results show a value of CO nearly one-tenth of the values obtained by Deutschmann et al. Moreover, both results indicate that CO is not produced on the surface, because the gradient of CO is nearly equal to zero, as can be seen from Fig. 6. The present level of CO is higher than the equilibrium value of CO at 1150 K, whereas the much higher levels of CO predicted by Deutschmann et al. cannot be justified as being produced by the gas-phase reactions or by the heterogeneous surface chemistry. This is because the present computations were carried out with the same surface chemistry as that used previously by Deutschmann et al. Although the present detailed gas reaction mechanism is not the same as that of Deutschmann et al., it is not conceivable that the difference can cause such a large discrepancy in CO mole fraction. It should be mentioned here that species that are produced on the catalytic surface have positive normal gradients at the gas–surface interface, whereas those being consumed have negative gradients. To unlock this mystery, the mass fraction of the carbon element was computed, from all species that contain carbon, for the present numerical results and for that of Deutschmann et al. The resulting carbon element mass fractions are presented in Fig. 7 as excess carbon percent. It is defined as the percentage of the local carbon mass fraction minus the carbon mass fraction in the fresh fuel–air mixture divided by the carbon mass fraction in the fresh fuel–air mixture. The numerical values of the excess carbon should be zero everywhere on and above the catalytic surface, except for the numerical-algorithm-generated errors. Uncertainty limits were computed to amend the excess carbon percent obtained from the published data of Deutschmann et al., as depicted in Fig. 7. The present results show a maximum error of 5% in carbon mass fraction, whereas the data of Deutschmann et al. gave a maximum error of about 18% of the same variable. At the catalytic surface, for which the error in the carbon data of Deutschmann et al. is $18 \pm 1\%$, the present error in the carbon element is only 3%. At a distance of 1.8 cm from the catalytic surface, the error in the Deutschmann et al. data is about $3 \pm 1\%$ carbon deficiency, whereas the present carbon mass is essentially in perfect balance with the incoming carbon in unburned methane. The error in the present carbon mass fraction is the outcome of a cumulative error of about 1% in each mass fraction of the carbon-containing species. A possible conclusion that can be drawn from the preceding discussions is that the present main species containing carbon (CO, CO_2, and CH_4) may be more accurate than the previous data of Deutschmann et al.. The main difference is essentially in CO, because the other species are in good agreement. It seems that the carbon monoxide surface and gas reactions need further in-depth investigation.

The temperature profile along the jet centerline is depicted in Fig. 8, which shows good agreement between the present jet-centerline temperature profile and its counterpart, predicted by Deutschmann et al. [4], near the surface, whereas away from the surface, the present temperature is slightly lower. This can be attributed to differences in gas physical properties and/or the handling of the transport by combined convection and molecular diffusion. The present results indicate lower transport above the surface due to the effect of thermal conduction, which acts against the incoming convection of the unburned fuel–air mixture, as shown in Fig. 8.

The comparisons of reactants' and products' mole fractions and the dimensionless jet-centerline velocity and temperature profiles for two values of Reynolds number, namely: $Re = 53.4$ ($V_{in} = 6$ cm/s) and $Re = 213.6$ ($V_{in} = 24$ cm/s), are shown in Figs. 9 and 10. As the

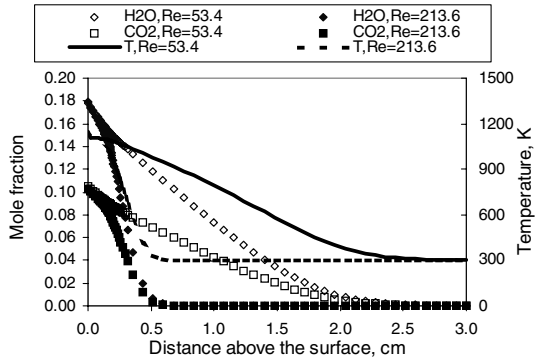

Fig. 10 Comparison of products' mole fractions and temperature profiles for $Re = 53.4$ ($V_{in} = 6$ cm/s) and $Re = 213.6$ ($V_{in} = 24$ cm/s), at 1150 K.

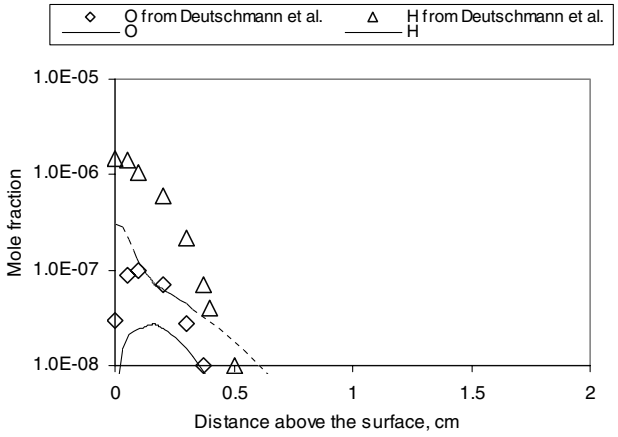

Fig. 11 Mole fractions of O and H above the surface and comparisons with results of Deutschmann et al. [4].

inlet jet velocity increases, the boundary layer is being squashed on the surface. This is an outcome of the upwind convection of the incoming gas mixture. However, the resulting shorter boundary layer can still consume the incoming methane as a consequence of the increased surface reaction rates imposed by the present new correlation of Eq. (13). At $Re = 53.4$, the gas-phase mole fractions' variations are limited to a distance of 2.5 cm above the catalytic surface. However, for $Re = 213.6$, the active boundary layer is squeezed into a distance of 0.7 cm above the catalytic surface, as can be seen from Fig. 9. Similarly, the products' mole fractions and temperature profiles, depicted in Figs. 9 and 10, indicate that as the Reynolds number increases from 53.4 to 213.6, the active boundary-layer thickness decreases from 2.5 to 0.7 cm above the catalytic surface.

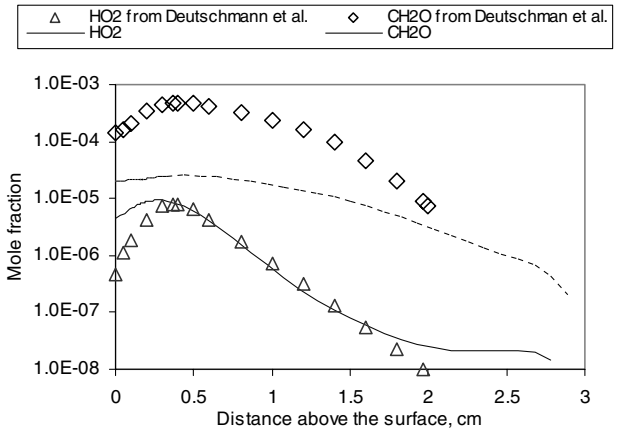

Fig. 12 Mole fractions of HO_2 and CH_2O above the surface and comparisons with results of Deutschmann et al. [4].

Figures 11 and 12 depict the axial profiles of some of the rare species produced by the combined effect of the heterogeneous surface and gas-phase reactions. The numerical data of Deutschmann et al. [4] agree qualitatively with the present mole fractions of H and O of Fig. 11 and HO_2 and CH_2O of Fig. 12. However, these species have extremely small values and better agreement cannot be expected unless the same gas-phase reaction mechanism is used. Most of these species are produced by the gas-phase reactions and hence have these peaks away from the catalytic surface. Moreover, the O atom is consumed in the catalytic surface, whereas the H atom is produced on the surface, as depicted in Fig. 11.

IV. Conclusions

The present paper describes a complete computational model for the prediction of the properties of reacting methane–air mixtures impinging over hot catalytic surfaces. For a surface temperature of 1150 K, the impinging gas mixture reacts mainly on the surface by the active uncovered platinum sites, which represent about 85% of the catalytic surface area. The computed surface production rates of the flowing gas phase show consistency with the stoichiometric coefficients of the main reacting species, in such a way that the consumption of CH_4 by 2 mol of O_2 produces approximately 1 mol of CO_2 and 2 mol of H_2O. This shows that the production of the rare species such as CH_3 and H_2O_2 is not appreciable, although they may be the main factors affecting the global reaction rate, as given by Eq. (13). New numerical correlations for the global reaction rate of CH_4 with O_2 and Sherwood number versus Reynolds number were deduced. As the Reynolds number increases, the Sherwood number and the surface reaction rate increase almost linearly. On the other hand, the active boundary-layer thickness decreased from 2.5 to 0.7 cm as the Reynolds number increased from 53.4 to 213.6, due to the reduced transport against the approaching gas mixture toward the catalytic surface. The analysis of the carbon mass fraction indicated that the predicted level of CO, although reasonable enough, still needs more investigation. The H atom is produced on the surface, whereas the O atom is consumed by catalytic reactions. The new correlations can be used as a global heterogeneous surface reaction submodel for the more complicated 3-D catalytic combustors.

References

[1] Williams, W. R., Stenzel, M. T., Song, X., and Schmidt, L. D., "Bifurcation Behavior in Homogeneous-Heterogeneous Combustion, 1: Experimental Results over Platinum," *Combustion and Flame*, Vol. 84, Nos. 3–4, 1991, pp. 277–291.

[2] Song, X., Williams, W. R., Schmidt, L. D., and Aris, R., "Bifurcation Behavior in Homogeneous-Heterogeneous Combustion, 2: Computations for Stagnation-Point Flow," *Combustion and Flame*, Vol. 84, Nos. 3–4, 1991, pp. 292–311.

[3] Warnatz, J., Allendorf, M. D., Kee, R. J., and Coltrin, M. E., "A Model of Elementary Chemistry and Fluid Mechanics in the Combustion of Hydrogen on Platinum Surfaces," *Combustion and Flame*, Vol. 96, No. 4, 1994, pp. 393–406.

[4] Deutschmann, O., Behrendt, F., and Warnatz, J., "Modeling and Simulation of Heterogeneous Oxidation of Methane on a Platinum Foil," *Catalysis Today*, Vol. 21, Nos. 2–3, 1994, pp. 461–470.

[5] Raja, L. L., Kee, R. J., Deutschmann, O., Warnatz, J., and Schmidt, L. D., "A Critical Evaluation of Navier-Stokes, Boundary-Layer, and Plug-Flow Models of the Flow and Chemistry in a Catalytic-Combustion Monolith," *Catalysis Today*, , Vol. 59, Nos. 1–2, 2000, pp. 47–60.

[6] Coltrin, M. E., Kee, R. J., and Rupley, F. M., "Surface Chemkin: A General Formalism and Software for Analyzing Heterogeneous Chemical Kinetics at a Gas–Surface Interface," *International Journal of Chemical Kinetics*, Vol. 23, No. 12, 1991, pp. 1111–1128.

[7] Abou-Ellail, M. M., Gosman, A. D., Lockwood, F. C., and Megahed, I. E. A., "Description and Validation of a Three-Dimensional Procedure for Combustion Chamber Flows," *Turbulent Combustion*, edited by L. Kennedy, Progress in Aeronautics and Astronautics, Vol. 58, AIAA, New York, 1978, pp. 163–190; *Journal of Energy*, Vol. 2, No. 2, 1978, pp. 71, 80.

[8] Tong, T. W., Abou-Ellail, M. M., Li, Y., and Beshay, K. R., "Numerical Computation of Reacting Flow in Porous Burners with an Extended CH4—Air Reaction Mechanism," HTFED04, 2004 ASME Heat Transfer/Fluids Engineering Summer Conference, Charlotte, NC, American Society of Mechanical Engineers Paper HT-FED 2004-56012, 2004.

[9] Peters, N., "Flame Calculations with Reduced Mechanisms," *Reduced Kinetic Mechanisms for Applications in Combustion Systems*, edited by Peters and Rogg, Lecture Notes in Physics, Springer–Verlag, New York, 1993.

[10] Peters, N., "Laminar Diffusion Flamelet Models in Non-Premixed Turbulent Combustion," *Progress in Energy and Combustion Science*, Vol. 10, No. 3, 1984, pp. 319–339.

[11] Kee, R. J., Rupley, F. M., and Miller, J. A., "The Chemkin Thermodynamic Data Base," Sandia National Laboratories, Rept. SAND87-8215B, Albuquerque, NM, 1996.

[12] Deutschmann, O., Maier, L. I., Riedel, U., Stroemman, A. H., and Dibble, R. W., "Hydrogen Assisted Catalytic Combustion of Methane on Platinum," *Catalysis Today*, , Vol. 59, Nos. 1–2, 2000, pp. 141–150.